PHOTONICS Research

Dynamically reconfigurable subwavelength optical device for hydrogen sulfide gas sensing

Zhengji Wen,[1] Jialiang Lu,[1] Weiwei Yu,[1] Hao Wu,[2] Hao Xie,[1] Xiaohang Pan,[1] Qianqian Xu,[1] Ziji Zhou,[1] Chong Tan,[1] Dongjie Zhou,[1] Chang Liu,[2] Yan Sun,[1,5] Ning Dai,[1,3] and Jiaming Hao[1,4,*]

[1]State Key Laboratory of Infrared Physics, Shanghai Institute of Technical Physics, Chinese Academy of Sciences, Shanghai 200083, China
[2]Key Laboratory of Artificial Micro- and Nano-structures of Ministry of Education, School of Physics and Technology, Wuhan University, Wuhan 430072, China
[3]Hangzhou Institute for Advanced Study, University of Chinese Academy of Sciences, Hangzhou 310024, China
[4]Institute of Precision Optical Engineering, School of Physics Science and Engineering, Tongji University, Shanghai 200092, China
[5]e-mail: sunny@mail.sitp.ac.cn
*Corresponding author: jiaming.hao@mail.sitp.ac.cn

Received 20 July 2021; revised 17 August 2021; accepted 21 August 2021; posted 24 August 2021 (Doc. ID 438095); published 29 September 2021

The importance of tunable subwavelength optical devices in modern electromagnetic and photonic systems is indisputable. Herein, a lithography-free, wide-angle, and reconfigurable subwavelength optical device with high tunability operating in the near-infrared regions is proposed and experimentally demonstrated, based on a reversible nanochemistry approach. The reconfigurable subwavelength optical device basically comprises an ultrathin copper oxide (CuO) thin film on an optical thick gold substrate by utilizing the reversible chemical conversion of CuO to sulfides upon exposure to hydrogen sulfide gas. Proof-of-concept experimental results show that the maximal modulation depth of reflectance can be as high as 90% at the wavelength of 1.79 μm with the initial thickness of CuO taken as 150 nm. Partially reflected wave calculations combined with the transfer matrix method are employed to analytically investigate the optical properties of the structure, which show good agreement with experimental results. We believe that the proposed versatile approaches can be implemented for dynamic control management, allowing applications in tunable photonics, active displays, optical encryption, and gas sensing.

https://doi.org/10.1364/PRJ.438095

1. INTRODUCTION

In recent years, active modulation of light has become an important driving force for progress with many emerging concepts and applications [1–3]. Different from passive nanostructures that usually exhibit fixed responses and cannot be dynamically altered once being fabricated [4–7], the emerging active tuning methods combined with various functional materials bring excellent tunability to optical systems [8–11]. A plethora of tuning mechanisms including electrical [12,13], thermal [14,15], optical [16], and mechanical stretching [17] have been put forward for designing reconfigurable devices with versatile functionality, ultrathin features, and easiness for integration. Such tunable devices could be achieved by employing active materials that can have their properties changed through exposure to external stimuli, such as phase change materials [18–23], liquid crystals [24–27], transparent conductive oxides [28–30], and semiconductors [31,32], and have been realized for various frequency regions. However, mastering dynamic spectral control in the near-infrared (NIR) remains a challenging task, mainly ascribed to unattainable functional materials at high frequencies [20].

In this work, we experimentally demonstrate a novel paradigm of lithography-free, wide-angle, and reconfigurable subwavelength optical devices with high tunability in the NIR regions, based on a reversible nanochemistry approach [33–39]. Our proposed reconfigurable optical device basically consists of an ultrathin, highly absorbing dielectric layer [copper oxide (CuO)] deposited on an optical opaque metallic substrate [gold (Au)], as shown in Fig. 1. The optical responses (high reflectance state/high absorption state) of the optical device were reconfigurable upon hydrogen sulfide exposure. In our design, a chemically responsive CuO material is chosen, mainly due to two factors: (1) it is a highly absorbing medium at visible and NIR wavelength regimes, which would benefit producing strong optical asymmetric Fabry–Pérot (FP)-type interference effects [40,41]; (2) as a pure p-type metal oxide semiconductor, it has a strong chemical affinity to acidic hydrogen sulfide (H_2S). There exists a reversible chemical conversion of CuO to sulfides upon exposure to H_2S contained air at certain temperatures, which would result in high optical tunability and offer unique ability to create chemiresistive gas sensors with enhanced performance [42]. It is noted that H_2S is a colorless,

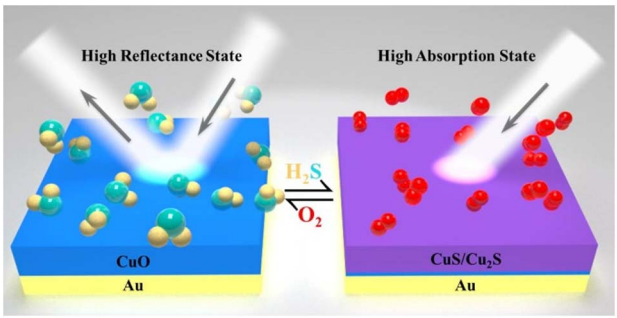

Fig. 1. Schematic of the lithography-free, wide-angle, and dynamically reconfigurable subwavelength optical device, composed of hydrogen sulfide responsive CuO thin films on an optical thick gold (Au) substrate by utilizing the reversible chemical conversion of CuO to sulfides (CuS/Cu_2S) upon exposure to H_2S contained air (O_2). The optical responses (high reflectance state/high absorption state) of the optical device were reconfigurable upon hydrogen sulfide exposure through phase-transition from CuO to CuS/Cu_2S.

flammable, and highly toxic gas, which has adverse effects on the human nervous and respiratory systems [43]. The development of novel optical devices for such noxious industrial gas sensing is strongly demanded for matters of work safety and process reliability [44]. From the application point of view, the proposed reconfigurable devices can be utilized to work as H_2S gas sensors. Relative reflection intensity response up to 90% was observed upon exposure to different volume concentrations of H_2S, which features great tunability and reconfigurability. Additionally, the operating wavelength can easily be tuned via adjusting structural parameters. Theoretical analyses not only confirm the rationality of experimental results, but also reveal that such a highly reconfigurable effect is ascribed to strong asymmetric FP effects in conjunction with the reversible chemical conversion of CuO to sulfides.

2. EXPERIMENT

A. Materials Preparation and Fabrication

Single-polished silicon (Si) substrates, each piece about 1.5 cm × 1.5 cm after cutting, were used in this work. After hydrophilic treatment in a piranha solution (volume ratio of H_2O_2 and H_2SO_4 of about 3:1), the Si wafers were soaked in the mixture for 30 min, and then ultrasonically cleaned by acetone, ethanol, and deionized water (19.3 MΩ) for 15 min, followed by drying with nitrogen gas.

The whole fabrication procedure of the reconfigurable subwavelength optical device is schematically depicted in Figs. 2(a_1)–2(a_5). We first deposited a 200 nm thick Au film on a cleaned Si wafer by thermal evaporation (PZF-300, KYKY), serving as a mirror to eliminate light transmission. To prevent the Au film from falling off by the lattice mismatch between the Au film and Si wafer, a 5 nm titanium (Ti) as an adhesive layer was deposited on the Si wafer before depositing

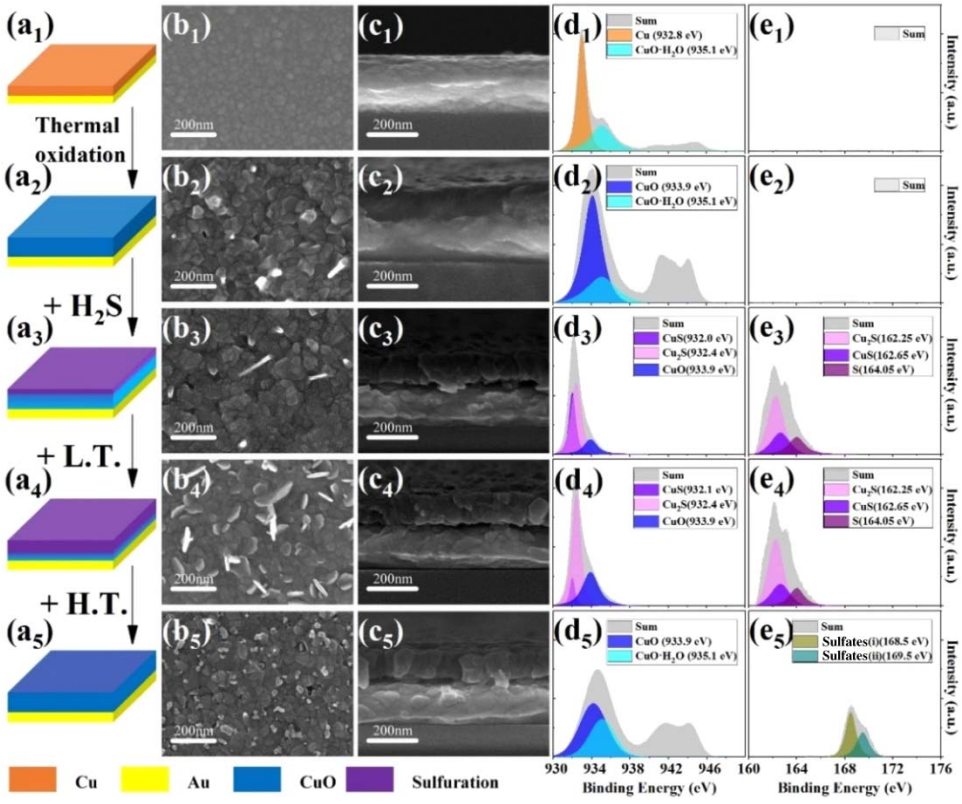

Fig. 2. (a_1)–(a_5) Schematic of the fabrication process of the proposed reconfigurable subwavelength optical device nanostructure. Here, L.T. denotes low temperature annealing at 40°C, and H.T. denotes high temperature annealing at 400°C. Corresponding surface (b_1)–(b_5) and cross-sectional (c_1)–(c_5) SEM images of the fabricated sample. Scale bars are 200 nm. Corresponding copper (Cu) element (d_1)–(d_5) and sulfur (S) element (e_1)–(e_5) spectra were detected by high-resolution XPS.

the Au layer. Then, five different thick copper (Cu) films (20, 40, 60, 80, and 100 nm) were sequentially deposited onto the Au film by a high vacuum double ion beam sputtering method (BAL-TEC, SCD 500). Next, the samples were placed on an LED constant temperature heating table (SET-217) in a muffle furnace for thermal oxidation annealing in air at 400°C for 2 h. In this process, the metallic Cu films were fully oxidized to CuO films with corresponding thicknesses of $d = 35$, 70, 110, 150, and 180 nm.

The prepared samples were then placed in a 5 mL centrifuge tube, followed by injecting H_2S (with ∼10% volume fraction in air) into it and then tightening it quickly after extracting the required volume of gas from the sampling bag by a needle. Next, the samples of the following three states were done in order: (1) the samples and H_2S fully reacted at 18°C for 5 min, (2) samples in step (1) were heated at 40°C for 5 min, and (3) samples in step (2) were heated at 400°C for 5 min. Accordingly, all of the samples were carried out several times to ensure repeatability.

B. Characterization and Measurements

Morphologies of the corresponding fabricated samples were characterized by a scanning electron microscope (SEM, FEI Sirion 200) on high-resolution mode with 200 nm scale bars. Figures 2(b_1)–2(b_5) and 2(c_1)–(c_5) show the surface/cross section SEM images of a fabricated sample before annealing (with 80 nm Cu film) and after annealing (with 150 nm CuO film), respectively. Figure 2(b_1) shows that the quality of the forming film was fairly good and thus the surface was smooth. A sharp interface between Si and Au is observed in Fig. 2(c_1), while there is no distinct boundary between Au and Cu. As shown in Fig. 2(b_2), granular crystallization on the surface appears, attributed to the recrystallization of Cu during the thermal oxidation process, resulting in a rough CuO surface. The thickness of the top layer is increased by a factor of ∼2, and stratified phenomena in the structure can be observed after Cu fully oxidizes to CuO [see Fig. 2(c_2)]. After injecting H_2S at room temperature (18°C) for 5 min, as shown in Figs. 2(b_3) and 2(c_3), the surface of the structure was covered by dense small particles along with apparent vulcanization, but had no obvious impact on thickness. After heating the sample at low temperature (40°C) for 5 min, promoted vulcanization is observed in Figs. 2(b_4) and 2(c_4), indicating there exists a conversion of copper sulfide (CuS) to cuprous sulfide (Cu_2S). Finally, the reconfigurable effects were realized at high temperature (400°C) for 5 min, as shown in Figs. 2(b_5) and 2(c_5). After high temperature caused vulcanization to be broken, the surface and cross section SEM images were generally restored to Figs. 2(b_2) and 2(c_2).

To investigate the elements of the corresponding nanolayer film, X-ray photoelectron spectroscopy (XPS, Thermo ESCALAB 250X) measurements using monochromated Al Kα X-rays ($h\nu = 1486.6$ eV) were performed. Cu element [Figs. 2(d_1)–2(d_5)] and S element [Figs. 2(e_1)–2(e_5)] spectra were detected with a resolution of 0.1 eV. As shown in Figs. 2(d_1) and 2(d_2), the Cu elements mainly exist in the form of metallic and adsorbed water combined copper-oxide. At these stages, as expected, no S element was detected. After injecting H_2S, it was found that the reaction product was mixed with CuS and Cu_2S, and partial copper-oxide and sulfur monomer are doped together [Figs. 2(d_3) and 2(e_3)]. As observed in Figs. 2(d_4) and 2(e_4), after low temperature (40°C) annealing, a similar characteristic affects just the distribution of the S elements, as compared to the last step. Finally, as shown in Figs. 2(d_5) and 2(e_5), after 5 min of high temperature (400°C) annealing, Cu element detection is restored to Fig. 2(d_2) with a small amount of sulfur remaining. All of these results confirm the structures as designed.

The experimental visible and NIR reflection spectra were recorded using a UV-VIS-NIR spectrophotometer (PerkinElmer Lamda 950). The angle-resolved infrared reflectance (absorbance) spectrum measurements were characterized using a Fourier transform infrared (FTIR, Bruker IFS 66 v/S) spectrometer for both TE- and TM-polarized light, equipped with a reflection module allowing for angles ranging from 13° to 80°. The measured reflectance spectra were normalized with respect to an Au mirror, and unpolarized reflectance was obtained by $R = (R_{TE} + R_{TM})/2$. Since the bottom Au film was thick enough to eliminate light transmission (T), the absorbance (A) can be calculated as $A = 1 - R$. For numerical simulations, the optical constants of Au were taken from the literature [45]. The refractive indices of CuO and CuS were extracted via ellipsometric measurements (see detailed optical parameters in Appendix A).

3. RESULTS AND DISCUSSION

Figures 3(a)–3(d) display the experimental reflectance spectra for four different thicknesses of CuO thin films ($d = 35$, 110, 150, and 180 nm) deposited on Au. It is noted that there exist very weak resonances for such cases, meaning that they can serve as the initial states (state i, black lines) of the reconfigurable devices. Next, after fully reacting with 4% (volume fraction) H_2S in air at room temperature for several minutes, the samples have pronounced amplitude changes in reflectance spectra (state ii, blue lines), due to the chemical conversion of CuO to sulfides as follows [42]:

$$CuO + H_2S \rightarrow CuS + H_2O, \quad (1)$$

$$CuO + H_2S \rightarrow 0.5\,Cu_2S + H_2O + 0.5\,S. \quad (2)$$

Reactions could happen simultaneously including chemical Eqs. (1) and (2) at room temperature. Low temperature annealing (40°C) of the films was then performed for further optimization, and the obtained results are shown in Fig. 3 marked as state iii (olive lines). Slight changes in the reflectance are observed, which can be attributed to the redistribution of the above two chemical reactions.

After high temperature annealing at 400°C (state iv, red lines), the reflectance nearly returns to the initial states (state i, black lines), mainly ascribed to the chemical conversion [42]

$$CuS + 1.5\,O_2 \rightarrow CuO + SO_2. \quad (3)$$

The corresponding theoretical reflectance spectra calculated by transfer matrix methods (TMMs) [46,47] are presented in Figs. 3(e)–3(h). Both experimental and theoretical data are found to be in good agreement, and show that the resonances can easily be tuned by adjusting the initial thickness of

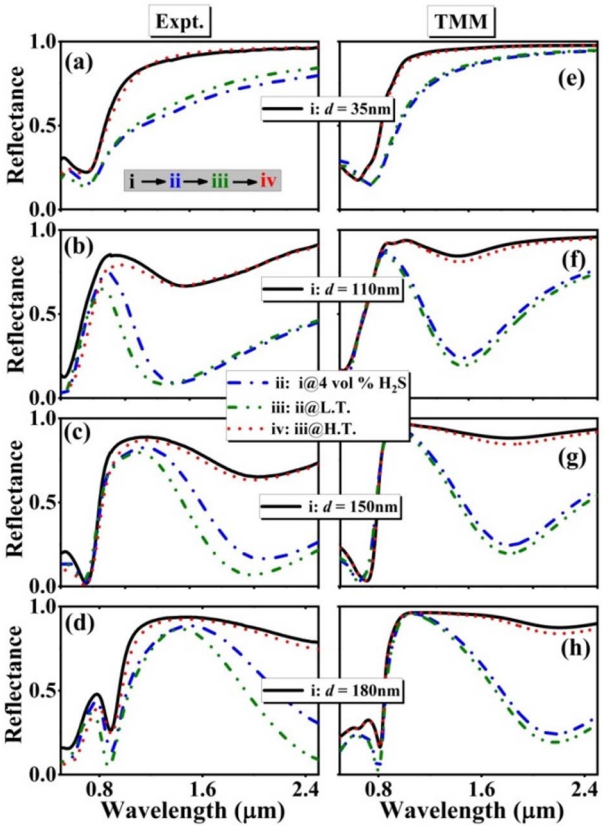

Fig. 3. (a)–(d) Experimental realization of reconfigurable subwavelength optical device when the initial thickness of the top CuO layer $d = 35$, 110, 150, and 180 nm, respectively. (e)–(h) Corresponding TMM calculated results of reflectance versus wavelength for the four cases. Both experimental and theoretical spectra are found to be in good accordance. State i: initial state as fabricated; state ii: fully reacting state; state iii: low temperature annealing state; state iv: high temperature annealing state.

CuO films. The slight difference between experimental and calculated optical reflectance spectra mainly results from random thickness fluctuations and diffusive intermixing at the interfaces [48–52]. It is noted that as the initial thickness of CuO thin films was taken as 150 nm [Fig. 3(c)], large tunability results can be achieved within the wavelength region of our interest; this is mainly due to the fact that the critical coupling conditions between the absorptive and radiative losses of this structure are matched [53–55].

We performed partially reflected wave calculations based on a multiple scattering model to further investigate the optical properties of our proposed subwavelength optical devices [40]. Figure 4 shows complex phasor diagrams of reflection coefficients for the structures at the four different states seen in Fig. 3(g) with the initial thickness of the top CuO layer $d = 150$ nm at the wavelength of 1.79 μm. After injecting H_2S and under low temperature annealing at 40°C, two-layer (Au/CuO) structures undergo chemical reaction and probably convert to three-layer (Au/CuO/sulfides) structure. Therefore, the total reflection coefficient (r) can be expressed as [46]

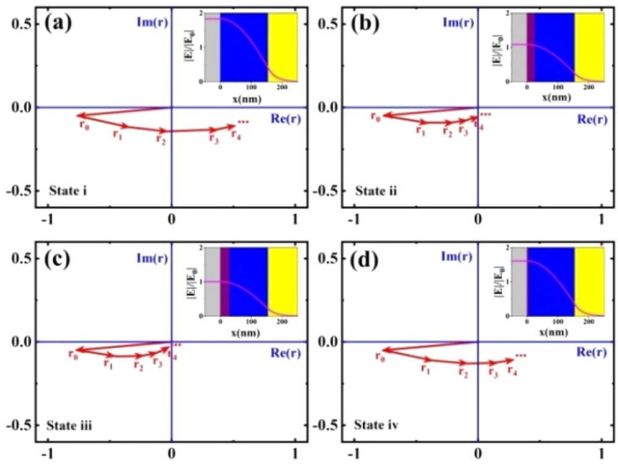

Fig. 4. Trajectory of sums of the calculated partially reflected waves for four different states studied in Fig. 3(g), with the initial thickness of the top CuO layer $d = 150$ nm. Insets are the corresponding normalized electric field amplitudes.

$$r = \frac{\tilde{r}_{01} + \tilde{r}_{12}e^{2i\tilde{\beta}_1} + \tilde{r}_{23}e^{2i\tilde{\beta}_2}(\tilde{r}_{01}\tilde{r}_{12} + e^{2i\tilde{\beta}_1})}{1 + \tilde{r}_{01}\tilde{r}_{12}e^{2i\tilde{\beta}_1} + \tilde{r}_{23}e^{2i\tilde{\beta}_2}(\tilde{r}_{12} + \tilde{r}_{01}e^{2i\tilde{\beta}_1})}, \quad (4)$$

where $\tilde{r}_{jk}$ denotes the Fresnel reflection coefficient for light incident from medium j to medium k, and $\tilde{\beta}_m$ is the phase propagating factors of layer m (here, $j, k, m = 0, 1, 2, \ldots$). The total reflection coefficients can also be expressed by the coherent sum of partially reflected waves $(r_0, r_1, r_2, \ldots)$, which can be expanded as [56,57]

$$r = r_0 + r_1 + r_2 + r_3 + \cdots = \sum_{n=0}^{\infty} r_n. \quad (5)$$

Here, r_n denotes the round-trip reflection coefficients (details of the partially reflected wave calculations are in Appendix B).

We know that when light is reflected from a highly absorbing layer on a metallic substrate, the phase of a complex reflection coefficient can deviate significantly from π, indicating that the phasor of partially reflected waves in the complex reflection coefficient diagram [Re(r) – Im(r)] is not along the conventional horizontal axis [Re(r)] [56]. The four phasor diagrams in Fig. 4 depict a clear trend in the complex phasor diagram, which are displayed as arrows and connected together head to tail. The final coordinate of the phasor diagram signifies the total reflection ($R = |r|^2$) and is related to the absorption ($A = 1 - R$). The first partially reflected wave r_0 always remains the same, because r_0 equals r_{01}, and thus there is no difference among these states. For states ii and iii, as shown in Figs. 4(b) and 4(c), the other partial waves $(r_1, r_2, r_3, \ldots)$ undergo anticlockwise rotation, and the amount of reflection phasors returns to the closet point of the origin, namely, these two states are almost reflectionless. For states i and iv, as shown in Figs. 4(a) and 4(d), the reflections are quite large, about 70%.

To provide further theoretical insight, electric field distributions inside the structure under the same conditions are investigated. As shown in the insets of Fig. 4, the corresponding

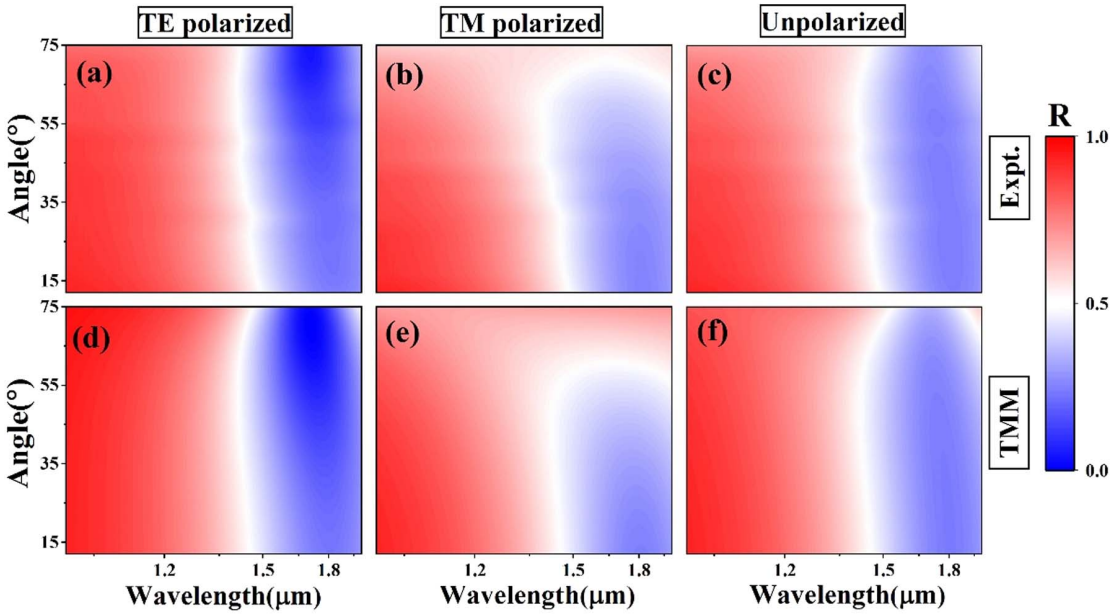

Fig. 5. (a)–(c) Experimental and (d)–(f) calculated reflectance mapping spectra as a function of wavelengths and incident angles for TE, TM, and unpolarized light, respectively. Here, initial thickness of the top CuO layer $d = 150$ nm upon exposure to 4% H_2S in air at L.T. at 40°C.

normalized electric field amplitudes are enhanced inside the absorbing film layer, which show excellent agreement with the partially reflected wave calculations. These calculations not only confirm that the asymmetric FP resonances indeed occur in these ultrathin films, but also verify the feasibility of our optical device, which possesses unique advantages for the design of a specific functional gas sensor. All of these results demonstrate that the feature of our subwavelength optical device indeed exhibits good reconfigurable properties, and highlight its potential application as a highly sensitive H_2S gas sensor.

Angular responses of the resonance effects were also investigated. Figures 5(a)–5(c) show the measured reflectance of the sample (here, 150 nm CuO film on state iii was chosen) as a function of wavelength and incident angle for TE, TM, and unpolarized light, respectively. The corresponding calculated reflectance spectra based on TMM are presented in Figs. 5(d)–5(f), and show good agreement with experimental results. Good angle-robust resonance performances are observed for all polarizations. This phenomenon is ascribed to the ultrathin feature of the structure with little phase accumulation; therefore, our optical devices are indeed very robust with respect to incident angles and polarizations. This unique angular-insensitivity characteristic of our subwavelength optical device indicates that it will have great potential in wide-angle sensing applications.

Finally, H_2S gas sensing tests upon exposure to different H_2S concentrations were carried out to verify the functionality of our subwavelength optical devices (see Fig. 6). The sensor was initially kept at two layers (Au/CuO) with 150 nm CuO, and then exposed to gas with H_2S concentration from 1% to 4% (volume fraction). To quantitatively analyze the reflection intensity change response of the target structures to H_2S exposure, we define the relative intensity change as [58]

$$\Delta R_{\mathrm{rel}} = \frac{|R_{\mathrm{i}} - R_{\mathrm{iii}}|}{R_{\mathrm{i}}} \times 100\%, \tag{6}$$

where R_{i} and R_{iii} represent the reflection of initial states i (black lines) and optimal state iii (olive lines), respectively. Note that the higher the volume fractions (within a given range), the larger the reflectance amplitude change that can be obtained [up to 90%, magenta lines in Fig. 6(d)] and finally saturated at a volume fraction of 4%. This prominent feature caused by the chemical conversion of CuO to sulfides can be explained by a percolation transition [Eqs. (1) and (2)]. As the concentration increases, the amount of sulfides reaches a certain critical plateau value

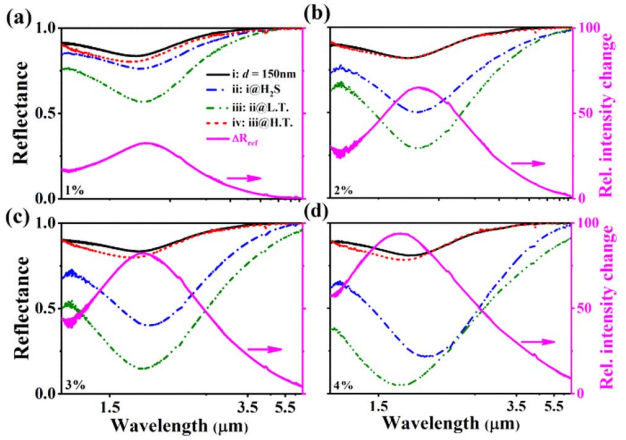

Fig. 6. Reflectance of the reconfigurable subwavelength optical device for different H_2S volume fractions of (a) 1%, (b) 2%, (c) 3%, and (d) 4% in air. Our sensor exhibits largest relative intensity change up to 90% (magenta lines) at 1.79 μm upon exposure to 4% H_2S in air. The increasing volume fractions lead to a pronounced relative intensity change of the reflectance spectrum.

and then tends to stable. It is worth mentioning that our gas sensor was able to reliably detect volume fractions down to 1% H_2S in air. Moreover, to verify the reliability of the experimental results, aging tests of the reflectance spectra at low concentrations of the corresponding four samples were also performed, which exhibit considerable long-term stability with almost invariable response in 20-day tests. The Au/CuO-based gas sensor exhibits good repeatability and long-term stability behavior (see Appendix C). All of these tests indicate that our reconfigurable gas sensor device performs quite well with high values of relative intensity response and offers great potential for high-performance H_2S gas sensing.

4. CONCLUSION

To summarize, we demonstrated a reconfigurable subwavelength optical device with simple planar thin-film stacks, which is composed of an ultrathin, highly absorbing CuO thin film on an optically thick gold substrate based on the reversible chemical conversion of CuO to sulfides. Experimental results show that our optical device exhibits a relative reflection amplitude modulation depth as high as 90% at the wavelength of 1.79 μm. Theoretical analyses show that the working mechanism of the wide-angle and highly tunable optical device is due to strong optical asymmetric FP thin-film resonance interference combined with reversible chemical conversion, and is found to be in good agreement with experimental results. Furthermore, to illustrate the versatility of the optical device, H_2S gas sensing tests were carried out, which exhibit high reconfigurability and good stability with very reproducible behavior. We anticipate that the proposed reconfigurable subwavelength optical device enables a broad avenue for developing active tuning and simple but sensitive optical gas sensors.

APPENDIX A: ELLIPSOMETRY DATA ANALYSES

We certify that the reconfigurable optical device is achieved by utilizing the reversible chemical conversion of CuO to CuS upon exposure to H_2S gas. To properly study the reflectance of the proposed devices, the optical constants of CuO and CuS were extracted by using spectroscopic ellipsometry. The complex refractive indices (n and k) derived from measured spectroscopic ellipsometric data are shown in Fig. 7. It is noted that, as expected, the extinction coefficient k increases sharply upon exposure to H_2S; this is related to strong optical asymmetric FP-type thin-film resonance interference, thus leading to the high absorption state seen in Fig. 1.

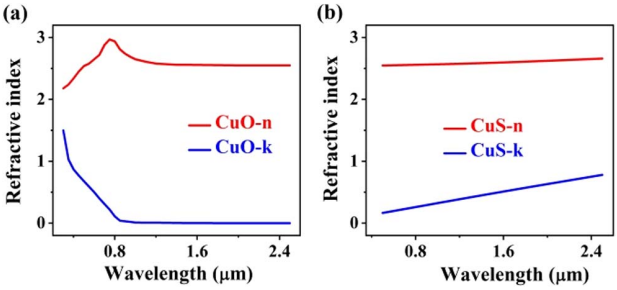

Fig. 7. Retrieved refractive indices (n) and extinction coefficients (k) of (a) CuO and (b) CuS thin films.

APPENDIX B: PARTIALLY REFLECTED WAVE CALCULATIONS

For a theoretical description of the physical mechanisms to achieve perfect absorption, as shown in Fig. 8, we consider light incident from air ($N_0 = 1$) upon one absorbing film 1 (CuS) with thickness h_1 and complex refractive index ($N_1 = n_1 + ik_1$), and another highly absorbing film 2 (CuO) with thickness h_2 and complex refractive index ($N_2 = n_2 + ik_2$), deposited on a metallic reflector (Au) with complex refractive index ($N_3 = n_3 + ik_3$) at angle θ. The reflection coefficient (r) of the structure calculated by a multiple scattering model can be written as follows [46]:

$$r = \tilde{r}_{0123} = \frac{\tilde{r}_{01} + \tilde{r}_{123}e^{2i\tilde{\beta}_1}}{1 + \tilde{r}_{01}\tilde{r}_{123}e^{2i\tilde{\beta}_1}}, \tag{B1}$$

where

$$\tilde{r}_{123} = \frac{\tilde{r}_{12} + \tilde{r}_{23}e^{2i\tilde{\beta}_2}}{1 + \tilde{r}_{12}\tilde{r}_{23}e^{2i\tilde{\beta}_2}}. \tag{B2}$$

Here, $\tilde{r}_{jk}$ denotes the Fresnel reflection coefficient for light incident from medium j to medium k, which is given by

$$\tilde{r}_{jk} = \begin{cases} \frac{N_j \cos\theta_j - N_k \cos\theta_k}{N_j \cos\theta_j + N_k \cos\theta_k} & \text{for TE polarization} \\ \frac{N_k \cos\theta_j - N_j \cos\theta_k}{N_k \cos\theta_j + N_j \cos\theta_k} & \text{for TM polarization} \end{cases} \tag{B3}$$

and

$$\tilde{\beta}_1 = \frac{2\pi}{\lambda} N_1 h_1 \cos\theta_1, \qquad \tilde{\beta}_2 = \frac{2\pi}{\lambda} N_2 h_2 \cos\theta_2. \tag{B4}$$

On the other hand, the reflection coefficient for such a system can be obtained by the coherent sum of the partially reflection waves, namely [56,57],

$$r = r_0 + r_1 + r_2 + r_3 + \cdots = \sum_{n=0}^{\infty} r_n, \tag{B5}$$

where r_i represents the round-trip reflection coefficient and can be written as

$$r_n = \begin{cases} \tilde{r}_{01} & \text{for } n = 0 \\ \tilde{t}_{01}\tilde{t}_{10}\tilde{r}_{123}^{n}\tilde{r}_{10}^{n-1}e^{2in\tilde{\beta}_1} & \text{for } n \geq 1 \end{cases}. \tag{B6}$$

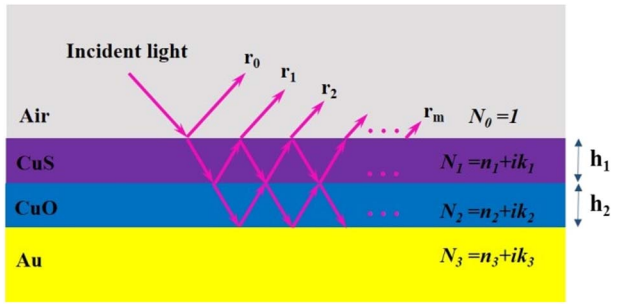

Fig. 8. Schematic illustration of light propagation in two subwavelength absorbing films on an optical opaque metallic reflector.

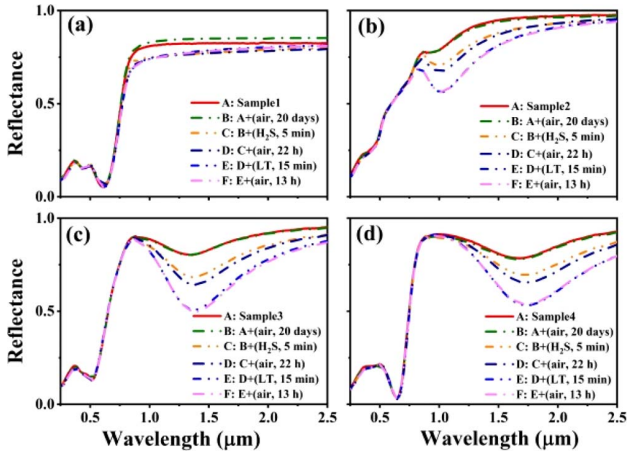

Fig. 9. Repeatability and stability tests of the reflectance spectrum for four different thicknesses of top CuO film samples with (a) 35 nm, (b) 110 nm, (c) 150 nm, and (d) 180 nm, upon exposure to 1% (volume fraction) H_2S in air.

Here, $\tilde{\tau}_{jk}$ denotes the Fresnel transmission coefficient for light incident from medium j to medium k, which is given by

$$\tilde{\tau}_{jk} = \begin{cases} \frac{2N_j \cos\theta_j}{N_j \cos\theta_j + N_k \cos\theta_k} & \text{for TE polarization} \\ \frac{2N_j \cos\theta_j}{N_k \cos\theta_j + N_j \cos\theta_k} & \text{for TM polarization} \end{cases}. \quad \textbf{(B7)}$$

Finally, the total reflectance can thus be obtained by

$$R = |r_0 + r_1 + r_2 + r_3 + \cdots|^2 = |r|^2. \quad \textbf{(B8)}$$

As shown in Fig. 4 in the main text, the final coordinate of the partial waves $(r_0, r_1, r_2, \ldots)$ phasor represents the total reflection R of the structure when the amount of the reflection phasor returns to the closet point of the origin, i.e., obtaining the largest absorption/tunability [see Fig. 4(c)].

APPENDIX C: REPEATABILITY AND STABILITY TESTS

To verify the robustness of the experimental gas sensing tests, low volume fractions down to 1% H_2S in air were performed for four different initial thicknesses of top CuO film samples (sample 1 at 35 nm, sample 2 at 110 nm, sample 3 at 150 nm, and sample 4 at 180 nm). As shown in Fig. 9, all four samples exhibit high reconfigurability and good stability with very reproducible behavior even after 20-day aging tests. It is noted that a relatively large reflectance amplitude change can be obtained on sample 3 with 150 nm CuO, which is in accordance with Fig. 3. All of these results show that our proposed gas sensor indeed possesses good repeatability and long-term stability behavior, which is crucial for practical applications.

Funding. National Key Research and Development Program of China (2017YFA0205800); National Natural Science Foundation of China (61471345, 62075231); Science and Technology Commission of Shanghai Municipality (20JC1414603); Shanghai Municipal Science and Technology Major Project (2019SHZDZX01); Shanghai Innovation Project (2021-cyxt1-kj04); Fundamental Research Funds for the Central Universities.

Disclosures. The authors declare no conflicts of interest.

Data Availability. Data underlying the results presented in this paper are not publicly available at this time but may be obtained from the authors upon reasonable request.

REFERENCES

1. O. Hess, J. B. Pendry, S. A. Maier, R. F. Oulton, J. M. Hamm, and K. L. Tsakmakidis, "Active nanoplasmonic metamaterials," Nat. Mater. **11**, 573–584 (2012).
2. J. Y. Ou, E. Plum, J. Zhang, and N. I. Zheludev, "An electromechanically reconfigurable plasmonic metamaterial operating in the near-infrared," Nat. Nanotechnol. **8**, 252–255 (2013).
3. Q. He, S. Sun, and L. Zhou, "Tunable/reconfigurable metasurfaces: physics and applications," Research **2019**, 1849272 (2019).
4. X. Liu, Z. Li, Z. Wen, M. Wu, J. Lu, X. Chen, X. Zhao, T. Wang, R. Ji, Y. Zhang, L. Sun, B. Zhang, H. Xu, J. Zhou, J. Hao, S. Wang, X. Chen, N. Dai, W. Lu, and X. Shen, "Large-area, lithography-free, narrow-band and highly directional thermal emitter," Nanoscale **11**, 19742–19750 (2019).
5. J. Hao, J. Wang, X. Liu, W. J. Padilla, L. Zhou, and M. Qiu, "High performance optical absorber based on a plasmonic metamaterial," Appl. Phys. Lett. **96**, 251104 (2010).
6. W. Zhao, Z. Wen, Q. Xu, Z. Zhou, S. Li, S. Fang, T. Chen, L. Sun, X. Wang, Y. Liu, Y. Sun, Y. W. Tan, N. Dai, and J. Hao, "Remarkable photoluminescence enhancement of $CsPbBr_3$ perovskite quantum dots assisted by metallic thin films," Nanophotonics **10**, 2257–2264 (2021).
7. X. Ruan, W. Dai, W. Wang, C. Ou, Q. Xu, Z. Zhou, Z. Wen, C. Liu, J. Hao, Z. Guan, and H. Xu, "Ultrathin, broadband, omnidirectional, and polarization-independent infrared absorber using all-dielectric refractory materials," Nanophotonics **10**, 1683–1690 (2021).
8. L. Kang, R. P. Jenkins, and D. H. Werner, "Recent progress in active optical metasurfaces," Adv. Opt. Mater. **7**, 1801813 (2019).
9. M. A. Mohammed, J. Melskens, R. Stabile, F. Pagliano, C. Li, W. M. M. Kessels, and O. Raz, "Metastable refractive index manipulation in hydrogenated amorphous silicon for reconfigurable photonics," Adv. Opt. Mater. **8**, 1901680 (2020).
10. A. Nemati, Q. Wang, M. Hong, and J. Teng, "Tunable and reconfigurable metasurfaces and metadevices," Opto-Electron. Adv. **1**, 18000901 (2018).
11. I. Kim, J. Yun, T. Badloe, H. Park, T. Seo, Y. Yang, J. Kim, Y. Chung, and J. Rho, "Structural color switching with a doped indium-gallium-zinc-oxide semiconductor," Photon. Res. **8**, 1381–1387 (2020).
12. J. Y. Ou, E. Plum, L. Jiang, and N. I. Zheludev, "Reconfigurable photonic metamaterials," Nano Lett. **11**, 2142–2144 (2011).
13. C. Meng, P. C. V. Thrane, F. Ding, J. Gjessing, M. Thomaschewski, C. Wu, C. Dirdal, and S. I. Bozhevolnyi, "Dynamic piezoelectric MEMS-based optical metasurfaces," Sci. Adv. **7**, eabg5639 (2021).
14. R. Singh, A. K. Azad, Q. X. Jia, A. J. Taylor, and H.-T. Chen, "Thermal tunability in terahertz metamaterials fabricated on strontium titanate single-crystal substrates," Opt. Lett. **36**, 1230–1232 (2011).
15. L. Lei, F. Lou, K. Tao, H. Huang, X. Cheng, and P. Xu, "Tunable and scalable broadband metamaterial absorber involving VO_2-based phase transition," Photon. Res. **7**, 734–741 (2019).
16. Y. Zhu, X. Hu, Y. Fu, H. Yang, and Q. Gong, "Ultralow-power and ultrafast all-optical tunable plasmon-induced transparency in metamaterials at optical communication range," Sci. Rep. **3**, 2338 (2013).
17. H. S. Ee and R. Agarwal, "Tunable metasurface and flat optical zoom lens on a stretchable substrate," Nano Lett. **16**, 2818–2823 (2016).
18. S. G.-C. Carrillo, A. M. Alexeev, Y.-Y. Au, and C. D. Wright, "Reconfigurable phase-change meta-absorbers with on-demand quality factor control," Opt. Express **26**, 25567–25581 (2018).

19. N. Mou, X. Liu, T. Wei, H. Dong, Q. He, L. Zhou, Y. Zhang, L. Zhang, and S. Sun, "Large-scale, low-cost, broadband and tunable perfect optical absorber based on phase-change material," Nanoscale **12**, 5374–5379 (2020).
20. Z. Zhu, P. G. Evans, R. F. Haglund, and J. G. Valentine, "Dynamically reconfigurable metadevice employing nanostructured phase-change materials," Nano Lett. **17**, 4881–4885 (2017).
21. Y. Wang, P. Landreman, D. Schoen, K. Okabe, A. Marshall, U. Celano, H. S. P. Wong, J. Park, and M. L. Brongersma, "Electrical tuning of phase-change antennas and metasurfaces," Nat. Nanotechnol. **16**, 667–672 (2021).
22. F. Ding, Y. Yang, and S. I. Bozhevolnyi, "Dynamic metasurfaces using phase-change chalcogenides," Adv. Opt. Mater. **7**, 1801709 (2019).
23. C. Ruiz de Galarreta, S. G. C. Carrillo, Y. Y. Au, E. Gemo, L. Trimby, J. Shields, E. Humphreys, J. Faneca, L. Cai, A. Baldycheva, J. Bertolotti, and C. D. Wright, "Tunable optical metasurfaces enabled by chalcogenide phase-change materials: from the visible to the THz," J. Opt. **22**, 114001 (2020).
24. D. Shrekenhamer, W. C. Chen, and W. J. Padilla, "Liquid crystal tunable metamaterial absorber," Phys. Rev. Lett. **110**, 177403 (2013).
25. S. Q. Li, X. Xu, R. M. Veetil, V. Valuckas, R. Paniagua-Domínguez, and A. I. Kuznetsov, "Phase-only transmissive spatial light modulator based on tunable dielectric metasurface," Science **364**, 1087–1090 (2019).
26. J. Li, P. Yu, S. Zhang, and N. Liu, "Electrically-controlled digital metasurface device for light projection displays," Nat. Commun. **11**, 3574 (2020).
27. I. Kim, W. S. Kim, K. Kim, M. A. Ansari, M. Q. Mehmood, T. Badloe, Y. Kim, J. Gwak, H. Lee, Y. K. Kim, and J. Rho, "Holographic metasurface gas sensors for instantaneous visual alarms," Sci. Adv. **7**, eabe9943 (2021).
28. J. Park, J. H. Kang, S. J. Kim, X. Liu, and M. L. Brongersma, "Dynamic reflection phase and polarization control in metasurfaces," Nano Lett. **17**, 407–413 (2017).
29. Y. Lee, J. Yun, S. J. Kim, M. Seo, S. In, H. D. Jeong, S. Y. Lee, N. Park, T. D. Chung, and B. Lee, "High-speed transmission control in gate-tunable metasurfaces using hybrid plasmonic waveguide mode," Adv. Opt. Mater. **8**, 2001256 (2020).
30. J. Park, B. G. Jeong, S. Il Kim, D. Lee, J. Kim, C. Shin, C. B. Lee, T. Otsuka, J. Kyoung, S. Kim, K. Y. Yang, Y. Y. Park, J. Lee, I. Hwang, J. Jang, S. H. Song, M. L. Brongersma, K. Ha, S. W. Hwang, H. Choo, and B. L. Choi, "All-solid-state spatial light modulator with independent phase and amplitude control for three-dimensional LiDAR applications," Nat. Nanotechnol. **16**, 69–76 (2021).
31. H. T. Chen, W. J. Padilla, J. M. O. Zide, A. C. Gossard, A. J. Taylor, and R. D. Averitt, "Active terahertz metamaterial devices," Nature **444**, 597–600 (2006).
32. P. C. Wu, R. A. Pala, G. K. Shirmanesh, W. H. Cheng, R. Sokhoyan, M. Grajower, M. Z. Alam, D. Lee, and H. A. Atwater, "Dynamic beam steering with all-dielectric electro-optic III–V multiple-quantum-well metasurfaces," Nat. Commun. **10**, 3654 (2019).
33. A. Tittl, P. Mai, R. Taubert, D. Dregely, N. Liu, and H. Giessen, "Palladium-based plasmonic perfect absorber in the visible wavelength range and its application to hydrogen sensing," Nano Lett. **11**, 4366–4369 (2011).
34. F. Sterl, N. Strohfeldt, R. Walter, R. Griessen, A. Tittl, and H. Giessen, "Magnesium as novel material for active plasmonics in the visible wavelength range," Nano Lett. **15**, 7949–7955 (2015).
35. M. Li, D. Liu, H. Cheng, L. Peng, and M. Zu, "Manipulating metals for adaptive thermal camouflage," Sci. Adv. **6**, eaba3494 (2020).
36. J. Karst, M. Hentschel, F. Sterl, and H. Giessen, "Liquid hydrogenation of plasmonic nanoantennas via alcohol deprotonation," ACS Photon. **8**, 1810–1816 (2021).
37. Y. Jin, L. Zhou, J. Liang, and J. Zhu, "Electrochemically driven dynamic plasmonics," Adv. Photon. **3**, 044002 (2021).
38. A. Böhme, F. Sterl, E. Kath, M. Ubl, V. Manninen, and H. Giessen, "Electrochemistry on inverse copper nanoantennas: active plasmonic devices with extraordinarily large resonance shift," ACS Photon. **6**, 1863–1868 (2019).
39. Y. Lee, J. Yun, M. Seo, S. J. Kim, J. Oh, C. M. Kang, H. J. Sun, T. D. Chung, and B. Lee, "Full-color-tunable nanophotonic device using electrochromic tungsten trioxide thin film," Nano Lett. **20**, 6084–6090 (2020).
40. H. Pan, Z. Wen, Z. Tang, G. Xu, X. Pan, Q. Xu, Y. Lu, H. Xu, Y. Sun, N. Dai, and J. Hao, "Wide gamut, angle-insensitive structural colors based on deep-subwavelength bilayer media," Nanophotonics **9**, 3385–3392 (2020).
41. M. A. Kats, R. Blanchard, P. Genevet, and F. Capasso, "Nanometre optical coatings based on strong interference effects in highly absorbing media," Nat. Mater. **12**, 20–24 (2013).
42. A. Paul, C. Weinberger, M. Tiemann, and T. Wagner, "Copper oxide/silica nanocomposites for selective and stable H_2S gas detection," ACS Appl. Nano Mater. **2**, 3335–3338 (2019).
43. S. K. Ganapathi, M. Kaur, R. Singh, V. I. Singh, A. K. Debnath, K. P. Muthe, and S. C. Gadkari, "Anomalous sensing response of NiO nanoparticulate films toward H_2S," ACS Appl. Nano Mater. **2**, 6726–6737 (2019).
44. K. Khaliji, S. R. Biswas, H. Hu, X. Yang, Q. Dai, S. H. Oh, P. Avouris, and T. Low, "Plasmonic gas sensing with graphene nanoribbons," Phys. Rev. Appl. **13**, 011002 (2020).
45. E. D. Palik, *Handbook of Optical Constants of Solids* (Academic, 1985).
46. P. Yeh, *Optical Wave in Layered Media* (Wiley, 1988).
47. Z. Wen, H. Xu, W. Zhao, Z. Zhou, X. Li, S. Li, J. Zhou, Y. Sun, N. Dai, and J. Hao, "Nonlocal effective-medium theory for periodic multilayered metamaterials," J. Opt. **23**, 065103 (2021).
48. R. Ravi and A. Paul, "Diffusion mechanism in the gold-copper system," J. Mater. Sci. Mater. Electron. **23**, 2152–2156 (2012).
49. S. Liu, Z. Sun, Q. Liu, L. Wu, Y. Huang, T. Yao, J. Zhang, T. Hu, M. Ge, F. Hu, Z. Xie, G. Pan, and S. Wei, "Unidirectional thermal diffusion in bimetallic Cu-Au nanoparticles," ACS Nano **8**, 1886–1892 (2014).
50. L. Lu, W. Dong, J. K. Behera, L. Chew, and R. E. Simpson, "Interdiffusion of plasmonic metals and phase change materials," J. Mater. Sci. **54**, 2814–2823 (2019).
51. A. B. Martin, R. D. Johnson, and F. Asaro, "Diffusion of gold into copper," J. Appl. Phys. **25**, 364–369 (1954).
52. J. Shields, C. R. de Galarreta, J. Bertolotti, and C. D. Wright, "Enhanced performance and diffusion robustness of phase-change metasurfaces via a hybrid dielectric/plasmonic approach," Nanomaterials **11**, 525 (2021).
53. H. A. Haus, *Waves and Fields in Optoelectronics* (Prentice-Hall, 1984).
54. S. Fan, W. Suh, and J. D. Joannopoulos, "Temporal coupled-mode theory for the Fano resonance in optical resonators," J. Opt. Soc. Am. A **20**, 569–572 (2003).
55. C. Qu, S. Ma, J. Hao, M. Qiu, X. Li, S. Xiao, Z. Miao, N. Dai, Q. He, S. Sun, and L. Zhou, "Tailor the functionalities of metasurfaces based on a complete phase diagram," Phys. Rev. Lett. **115**, 235503 (2015).
56. B. H. Woo, I. C. Seo, E. Lee, S. Y. Kim, T. Y. Kim, S. C. Lim, H. Y. Jeong, C. K. Hwangbo, and Y. C. Jun, "Dispersion control of excitonic thin films for tailored superabsorption in the visible region," ACS Photon. **4**, 1138–1145 (2017).
57. M. A. Kats, D. Sharma, J. Lin, P. Genevet, R. Blanchard, Z. Yang, M. M. Qazilbash, D. N. Basov, S. Ramanathan, and F. Capasso, "Ultra-thin perfect absorber employing a tunable phase change material," Appl. Phys. Lett. **101**, 221101 (2012).
58. C. U. Hail, A. K. U. Michel, D. Poulikakos, and H. Eghlidi, "Optical metasurfaces: evolving from passive to adaptive," Adv. Opt. Mater. **7**, 1801786 (2019).